THE JOURNAL OF PHYSICAL CHEMISTRY B
A JOURNAL OF THE AMERICAN CHEMICAL SOCIETY

pubs.acs.org/JPCB

Article

# Cage Dynamics-Mediated High Ionic Transport in Li-$O_2$ Batteries with a Hybrid Aprotic Electrolyte: LiTFSI, Sulfolane, and *N*,*N*-Dimethylacetamide

Dhananjay and Bhabani S. Mallik*

Cite This: *J. Phys. Chem. B* 2023, 127, 2991−3000

Read Online

ACCESS | Metrics & More | Article Recommendations

**ABSTRACT:** Mixed electrolytes perform better than single solvent electrolytes in aprotic lithium-$O_2$ batteries in terms of stability and transportation. According to an experimental study, a mixed electrolyte consisting of dimethylacetamide (DMA)/sulfolane (TMS) with lithium bisfluorosulfonimide (LiTFSI) showed high ionic conductivity, oxygen solubility, remarkable stability, and better cycle life than only DMA-based or TMS-based electrolytes. In this work, we used classical molecular dynamics simulations to explore the structure and ionic dynamics of the DMA/TMS hybrid electrolytes at two compositions. We calculated radial, combined, and spatial distribution functions for the structural examination. These properties depict a minimal change in the electrolyte structure by increasing the DMA content in the electrolyte from 20 to 50% by volume. We used the diffusive regimes from mean square displacements for diffusion coefficient calculations. Ionic conductivities calculated using the Green−Kubo equation have an acceptable agreement with the experimental values, whereas the Nernst−Einstein relation is found insufficient to explain the ionic transport. The relatively lower value of the ion-cage lifetime of electrolyte components with 50% DMA shows their faster dynamics. Moreover, we present the new physical insight by focusing on ion-pair and ion-cage formation and their correlation with ionic conductivity. The atomic-level understanding through this work may assist in designing electrolytes for aprotic Li-$O_2$ cells.

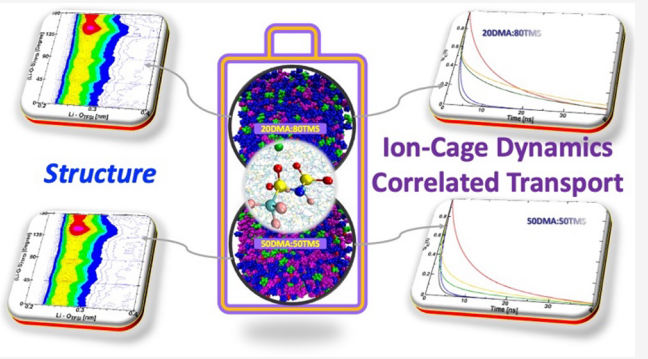


## 1. INTRODUCTION

In the growing technical world, there is a need for well-functioning electrical energy storage systems for the development of portable electronic devices and hybrid electric vehicles.[1,2] Apart from conventional energy storage systems like lithium-ion batteries and supercapacitors, lithium-air batteries are emerging as a practical storage device for the future because of their extreme theoretical specific energy compared to Li-ion batteries.[3] Out of different categories of lithium-air batteries, the aprotic Li-$O_2$ system[4,5] got colossal attention from the researcher's community. Despite promising specific energy, this battery system has several technical hurdles to cross over. Aside from significant challenges, like formulation of efficient catalysts[6−8] for the cathodic surface, dendrite growth at the anode, and stabilization of the desired cathodic product (i.e., $Li_2O_2$), the instability of the electrolytes equally contributes toward the non-commercialization of the aprotic Li-$O_2$ batteries.[3,9] A suitable electrolyte for these devices can reduce the problems mentioned above and improve the dynamic properties, such as diffusion and conductivity, which can play a crucial role in making the Li-$O_2$ battery a truly rechargeable efficient device.

Different varieties of aprotic electrolytes have been investigated in the last several years.[10] In the early research on the electrolytic components of aprotic Li-$O_2$ devices, organic carbonates were mostly the focus.[11−14] But carbonates are chemically unstable toward the intermediate (i.e., superoxide $O_2^{\cdot-}$ radical) formed during the discharge process. The nucleophilic attack of $O_2^{\cdot-}$ on carbonates gives lithium alkyl carbonates (RCOOLi), $Li_2CO_3$, $H_2O$, $CO_2$, etc., instead of $Li_2O_2$.[12,14,15] Consequently, there is a need to move toward other aprotic solvents to construct a suitable electrolyte. Ethers (e.g., tetraglyme) are better solvents than organic carbonates; they are more stable toward the reactive $O_2$ intermediate than carbonates. But, still, they undergo decomposition to give various unwanted products.[16,17] Researchers also explored many ionic liquids as electrolytes for lithium-air batteries.[18−20]

**Received:** November 7, 2022
**Revised:** February 9, 2023
**Published:** March 24, 2023

They have been relatively safer solvents for the active superoxide species. However, with the high viscosity of ionic liquids, the mobility of Li-ions is affected, resulting in low conductivity compared to organic electrolytes. They have relatively low solubility and diffusivity of oxygen. Based on the results from cyclic voltammetry and computational studies,[21] nitrogen-based solvents, like amides, nitriles, and lactams, are the better option for lithium-air electrolytes. Linear alkyl amides, like dimethylacetamide (DMA), were very stable toward the oxygen reduction species,[22] but solvents of this family are unable to form a solid electrolyte interface (SEI) at the anodic terminal. However, the salt $LiNO_3$ and the fluorinated amides as additives stabilized the SEI.[22,23] Similarly, despite being stable against $O_2$-active species, solvents like acetonitrile, phosphate, and siloxane are also reactive toward the Li electrode. Several groups have studied electrolytes based on DMSO[24−26] and shown their suitability for the Li-$O_2$ system as it has better oxygen diffusivity, conductivity, and sensational stability toward superoxide. However, the increasing number of cycles undergoes decomposition and poor battery performance. These solvents also interact with the Li-electrode and show a low-cycling tendency.[27,28] Moreover, the vapor pressure of DMSO is not low enough. Hence, DMSO demonstrates partial fulfillment for this battery. In the family of sulfones, sulfolane (TMS) gave better results for lithium-air cells, confirmed by experimental[29−31] and quantum mechanical-based[21] studies. This dipolar aprotic solvent has high electrochemical stability. It is even stable while operating at a voltage of more than 4.5 V. TMS has remarkable cycling performance, much better than DMSO and many others. Also, the five-membered cyclic structure contributes sulfolane to construct a genuine rechargeable Li-$O_2$ battery. But the problem with this solvent is that it stays in the solid state at room temperature; therefore, it results in low mobility of $Li^+$ and possesses slower dynamics than organic electrolytes.

Of the above-addressed electrolytes, none is ideal for lithium-oxygen batteries according to the requirements—better stability and conductivity. Therefore, the scientific community has been designing the above-described solvents to give a further edge to forming different mixed electrolytes. Earlier studies[32−36] showed the exclusive functioning of mixed electrolytes over single electrolytes in various aspects of the Li-$O_2$ device. Recently, Wang and coworkers reported[36] a binary hybrid electrolyte for the aprotic lithium-air cell. This electrolytic system has stable TMS and high-conducting DMA with LiTFSI as the salt. They investigated two compositions, 20:80 and 50:50 (% v/v) mixtures of DMA:TMS in 1 M LiTFSI. The increase in the DMA percentage decreases the mixture's viscosity, resulting in the fast transport of the Li-ion and enhanced ionic conductivity as well. The authors confirmed the fair oxygen solubility, high stability, and relatively much better cycling performance than TMS-based or DMA-based electrolytes. In this work, our investigation aims to uncover the structure and dynamical properties of the above-described compositions of DMA/TMS (20:80 and 50:50) mixed solvent in 1 M LiTFSI with the help of classical molecular dynamics (MD) simulations. We examine the changes in the solvation structure and transport properties with the increasing amount of DMA in the electrolyte. We use experimental data[36] to compare the ionic conductivities. Moreover, we present the new physical insight by focusing on ion-pair and ion-cage formation and their correlation with ionic conductivity.

## 2. COMPUTATIONAL METHOD

The chemical entities considered for this study are shown in Figure 1, with snapshots of the simulation boxes. The chemical

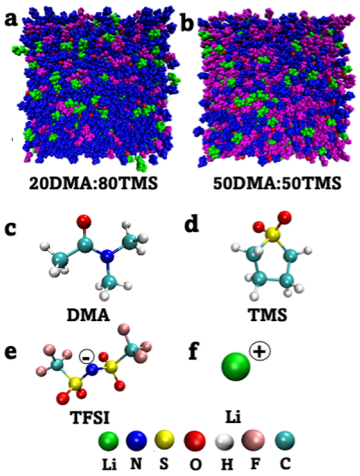


**Figure 1.** (a, b) Snapshots from the simulation box of both the electrolytes (blue = TMS, magenta = DMA, red = $Li^+$, and green = $TFSI^-$). Chemical species of the electrolytes: (c) *N*,*N*-dimethylacetamide = DMA; (d) tetramethyl sulfone = TMS; (e) bisfluorosulfonimide = $TFSI^-$; and (f) lithium-ion = $Li^+$.

entities (Figure 1c−f) were filled into the cubical box using Packmol[37] with 0.2 nm tolerance. The system with 20DMA:80TMS contains 433 LiTFSI, 3633 TMS, and 934 DMA units. The system with 50DMA:50TMS has 430 LiTFSI, 2252 TMS, and 2318 DMA units. The structure of each entity was obtained from the geometry optimization with the B3LYP method[38−40] and 6-311+G(2d,p) basis set using the Gaussian 09 package.[41] We used GROMACS 5.0.4[42,43] to perform MD simulations. We have used Optimized Potentials for Liquid Simulations-All Atom (OPLS-AA)[44] force field parameters for bonded and nonbonded interactions.[45] Nonbonded parameters of $Li^+$ were taken from Lee and Rasaiah's work.[46] To fit the charges on individual ions, we used the RESP method[47] available in the Antechamber package[48] and scaled the charges to 0.8. A particle-mesh Ewald method with a cutoff distance of 1.2 nm was used for the long-range electrostatic interactions, and a grid spacing of 0.1 nm was used for van der Waals interactions. Energy minimization was performed to relax the strained contacts in the initial configuration with the steepest descent minimization algorithm. All systems were heated at 500 K for 2 ns, and subsequent annealing was performed to have the final temperature of 300 K in 5 steps each for 2 ns. Afterward, isothermal-isobaric (NPT) equilibration was performed on the annealed systems for 50 ns with 1 fs time steps at 300 K temperature and 1 bar pressure to obtain the correct density for all the systems. After finding the equilibrated density, the isothermal-isochoric (NVT) equilibration was performed for 50 ns with 1 fs time steps. The V-rescale[49] thermostat and the Berendsen barostat[50] algorithms were used for the temperature and pressure control, respectively. The time constants for thermostat and barostat are 2 and 1 ps, respectively. We performed an NVE run for 100 ns with a time step of 1 fs for the production run. We generated the NVE trajectory by writing positions and velocities at every 2 ps, employed for all the analysis except conductivity. We performed another 1 ns of simulation within


https://doi.org/10.1021/acs.jpcb.2c07829
J. Phys. Chem. B 2023, 127, 2991−3000

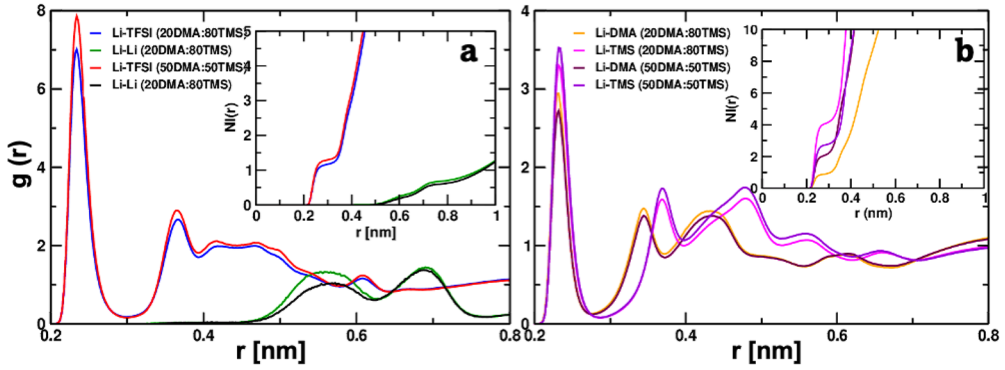


**Figure 2.** COM RDFs and number integrals (NI) of (a) Li-TFSI and Li-Li and (b) Li-TMS and Li-DMA.

the same ensemble, and the velocities at every time step were collected for the Green−Kubo integral.

## 3. RESULTS AND DISCUSSION

**3.1. Density and Structure of Electrolytes.** The average density of both electrolytes is calculated using the NPT simulations. The electrolyte density with 20% DMA is 1314.32 kg $m^{-3}$, and that of 50% DMA is 1224 kg $m^{-3}$; the percentage errors in densities are 1.8 and 1.0%, respectively, as compared to experimental results. The former has a higher density because (a) it has more TMS molecules having a higher molecular weight than DMA and (b) the unique five-membered cyclic structure of TMS does a better packing in the electrolyte solution. We investigated the center of mass (COM) RDFs of Li-TFSI and Li-solvent pairs for structural exploration of the electrolytic compositions, as shown in Figure 2. Figure 2a depicts that the TFSI ion appears at a distance of 0.23 nm from $Li^+$ and its occurrence decreases slightly on increasing the DMA content from 20 to 50%. But the first minima (0.3 nm) and the maxima (0.23 nm) of Li-TFSI pairs do not change with changing the composition; this shows that the interactions between ion pairs remain almost unchanged on changing the DMA content. The first peaks of cation−cation RDFs are spotted at the most extended distances with very short peak heights at 0.57 and 0.55 nm for 20DMA:80TMS and 50DMA:50TMS, respectively; moreover, their first minima lie at 0.77 and 0.76 nm with no alteration due to compositional change. The cation−cation interactions are significantly less pronounced due to the repulsive Coulombic effect; as a result, the remaining electrolytic species stay around $Li^+$ solvation shells.

The solvents have crucial contributions to the solvation process.[51] The organic solvents, DMA and TMS, used here majorly solvate the cation rather than the TFSI anion. Figure 2b shows that TMS and DMA both have the maximum probability of appearing at the same distance of 0.23 nm from the reference cation with no alteration due to an increase in the DMA content in the electrolyte. However, there is a slight increase in TMS occurrence and a negligible decrease in DMA occurrence on changing the electrolytic composition from 20DMA:80TMS to 50DMA:50TMS. The first minima for both Li-TMS and Li-DMA remain unchanged at 0.28 and 0.27 nm for both electrolytes. All the COM RDFs show oscillatory behavior. Table 1 shows that the correlations between Li and TFSI, Li and TMS, and Li and DMA in terms of first maxima, first minima, and first peak height remain almost similar for both electrolyte systems.

**Table 1. Effect of the Change in the Composition of Solvents on Maxima ($r_{max}$), First Peak Height $g(r_{max})$, Minima ($r_{min}$), and Coordination Number (CN) = NI ($r_{min}$) of COM RDFs**

| | pair | $r_{max}$ [nm] | $g(r_{max})$ | $r_{min}$ [nm] | NI($r_{min}$) |
|---|---|---|---|---|---|
| 20DMA:80TMS | Li-TFSI | 0.23 | 7.00 | 0.30 | 1.17 |
| | Li-TMS | 0.23 | 3.30 | 0.28 | 4.08 |
| | Li-DMA | 0.23 | 2.94 | 0.27 | 0.87 |
| 50DMA:50TMS | Li-TFSI | 0.23 | 7.86 | 0.30 | 1.29 |
| | Li-TMS | 0.23 | 3.52 | 0.28 | 2.74 |
| | Li-DMA | 0.23 | 2.72 | 0.27 | 2.04 |

Although the first maxima of COM RDFs of Li-TFSI and Li-solvents lie at the same distance, the peak height of Li-TFSI is the highest among all, with a considerable difference; this emphasizes the most occurrence of $TFSI^-$ around $Li^+$. The ion-pair and ion-cage lifetime value of Li-TFSI also supports it, as presented in the later sections. We also computed the coordination numbers (CNs) to know the number of anions/solvent molecules around the cation from the corresponding COM RDFs. The first minimum of the corresponding RDFs is the cutoff range for CN calculation. Here, we considered 0.3 nm as the cutoff distance for the first solvation shell of all RDFs. For DMA/TMS (20:80), the CNs of TFSI, TMS, and DMA in the first solvation shell around $Li^+$ are 1.17, 4.08, and 0.87, while these are 1.29, 2.74, and 2.04 in the DMA/TMS (50:50) electrolyte, respectively. In the 50DMA:50TMS electrolyte, the number of TMS molecules is less than DMA, but the number of TMS molecules contributing to the first solvation shell is greater than DMA; this emphasizes the better packing efficiency of TMS molecules than DMA around the $Li^+$.

We calculated the combined distribution functions (CDFs)[52] to get insight into the radial and angular orientations of various moieties. Figure 3 shows the CDFs between two RDFs, whereas combinations between angular distribution functions (ADFs) and RDFs are shown in Figure 4. Figure 3a,b indicates the CDF constituting RDF of $Li^+$ and $O_{TFSI}{}^-$ and RDF of $Li^+$ and N of the same $TFSI^-$. In DMA/TMS (20:80), the probable distance of $N_{TFSI}{}^-$ is ∼0.4 nm when $O_{TFSI}{}^-$ is at a distance of 0.22 to 0.24 nm from $Li^+$. But, in DMA/TMS (50:50), the more intense peak is found with a slight increase in the N atom distance from the cation, keeping the O position unchanged. Moreover, the contour plots also show the different coordinating fashions of O and N atoms from $TFSI^-$. In CDF plots of Figure 3c,d, the first probable distribution indicates the distance between $Li^+$ and O of TMS,


https://doi.org/10.1021/acs.jpcb.2c07829
J. Phys. Chem. B 2023, 127, 2991−3000

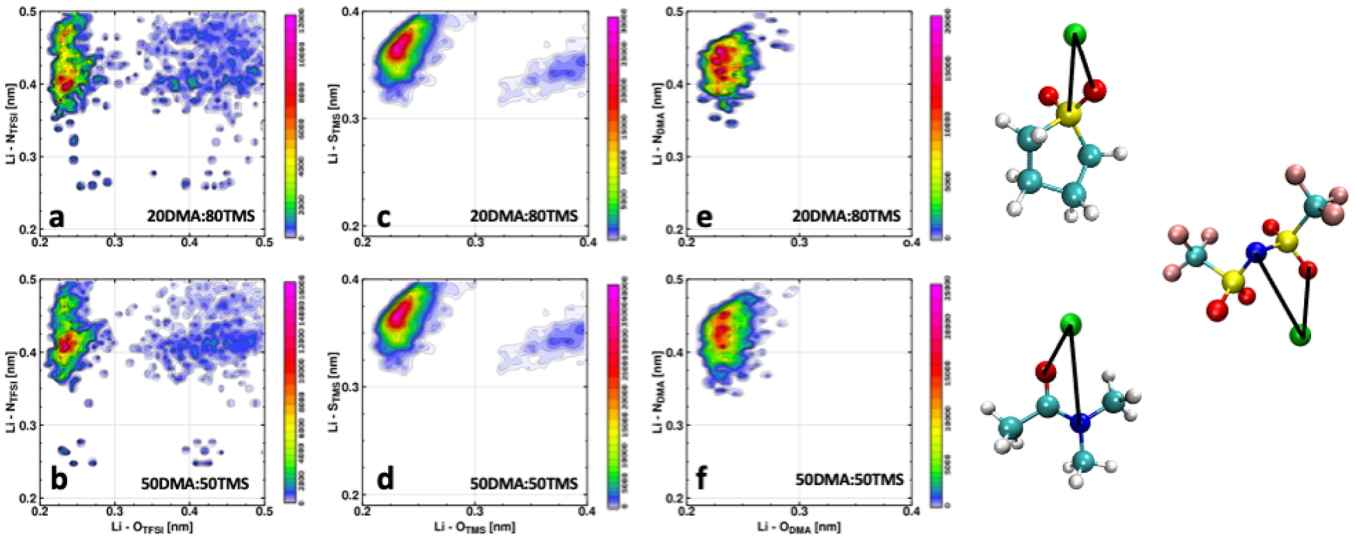


**Figure 3.** Combined radial−radial distribution functions between (a, b) Li-$O_{TFSI}$ and Li-$N_{TFSI}$, (c, d) Li-$O_{TMS}$ and Li-$S_{TMS}$, and (e, f) Li-$O_{DMA}$ and Li-$N_{DMA}$. Panels (a, c, and e) for 20DMA:80TMS and panels (b, d, and f) for 50DMA:50TMS.

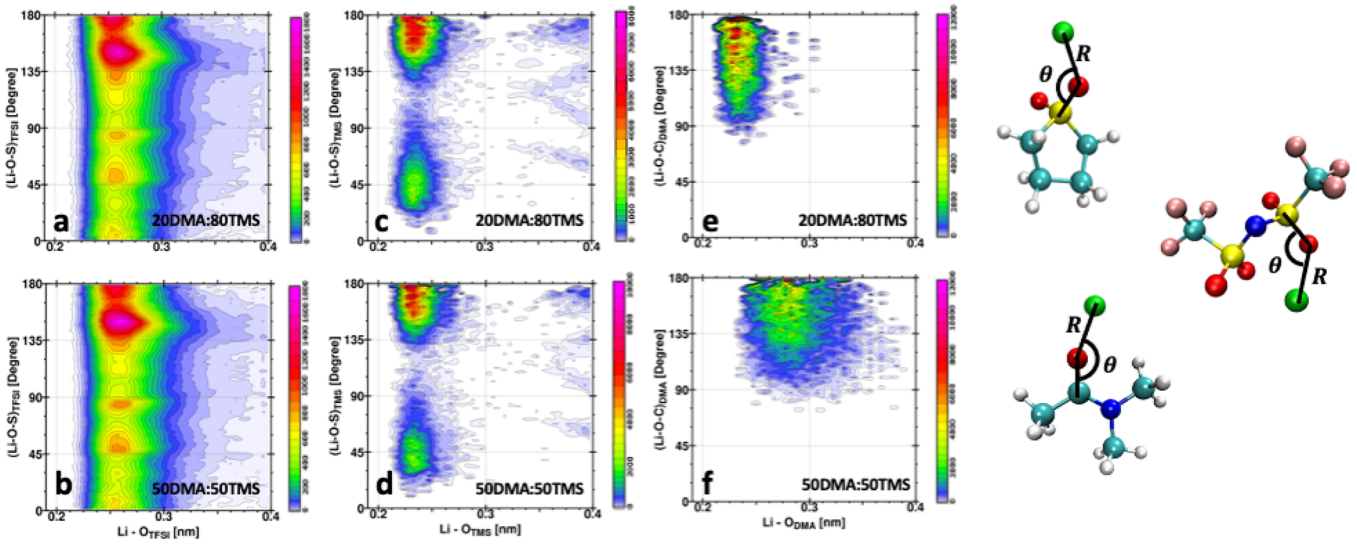


**Figure 4.** Combined radial−angular distributions between the (a, b) Li-$O_{TFSI}$ distance and $(Li\text{-}O\text{-}S)_{TFSI}$ angle, (c, d) Li-$O_{TMS}$ distance and $(Li\text{-}O\text{-}S)_{TMS}$ angle, and (e, f) Li-$O_{DMA}$ and $(Li\text{-}O\text{-}C)_{DMA}$. Panels (a, c, and e) for 20DMA:80TMS and panels (b, d, and f) for 50DMA:50TMS.

and the second one indicates the distance between $Li^+$ and S of the same TMS molecule. For both electrolytes, the most probable peak at $Li^+$-$O_{TMS}$ = 0.23 nm/$Li^+$-$S_{TMS}$ = 0.37 nm remains the same. The contour distribution between the cation and DMA is shown in Figure 3e,f. Both RDFs are defined by $Li^+$-$O_{DMA}$ and $Li^+$-$N_{DMA}$ (same DMA molecule) in these two CDF plots. The main peak in both the CDFs appears around 0.23/0.44 nm depicting the stronger coordination of $O_{DMA}$ than $N_{DMA}$ around $Li^+$, but the most probable distribution in Figure 3e is slightly more intense than that of Figure 3f.

Figure 4a,b demonstrates the CDF of angle $\theta$ (between Li-O and O-S vectors) and distance ($R$) between $Li^+$ and O of $TFSI^-$. Here, we have taken the average of all four-oxygen atoms of the anion. In both the CDFs, the most probable angle is 150°, which lies around 0.26 nm. This shows that the cation and the anion are oriented in a similar configuration in both 20DMA:80TMS and 50DMA:50TMS systems. The CDFs between the RDF of $Li^+$-$O_{TMS}$ and the corresponding Li-O-S angle are shown in Figure 4c,d. The contour plots indicate that the angle can lie between 150 and 180° when the $O_{TMS}$ is at ∼0.23 nm from $Li^+$. We observe similar arrangements of TMS molecules around the reference cation in both solutions. The probability distribution between the RDF of $Li^+$-$O_{DMA}$ and the corresponding Li-O-C angle for DMA/TMS (20:80) shows that the possible angle range is 170 to 180°, with the Li-$O_{DMA}$ distance of around 0.23 nm (Figure 4e). In contrast, for DMA/TMS (50:50), Figure 4f shows that the most probable Li-O-C angle lies near 180° with a $Li^+$-$O_{DMA}$ distance of 0.28 nm; this indicates a slight change in the orientation of DMA molecules around the reference cation on increasing the DMA content to 50% in the electrolytic solution.

Apart from RDFs and CDFs, we have calculated the spatial distribution functions (SDFs) of cations around anions and solvents using TRAVIS software,[52] as shown in Figure 5. SDFs computed around electrolytic components of 20DMA:80TMS have similar distributions as that of 50DMA:50TMS electrolytic species. The cation is mainly distributed around $O_{TFSI}$, with a small distribution around $N_{TFSI}$. The SDFs of $Li^+$



https://doi.org/10.1021/acs.jpcb.2c07829
J. Phys. Chem. B 2023, 127, 2991−3000

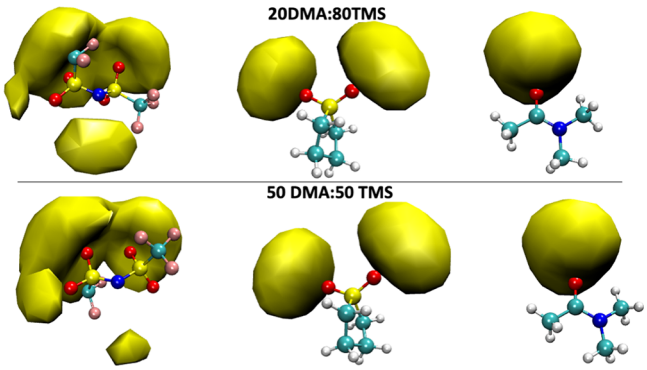


**Figure 5.** Spatial distribution functions of the cation around the TFSI anion, TMS, and DMA with iso value = 1.5.

around TMS and DMA also conclude the strong interaction of $O_{TMS}$ and $O_{DMA}$ with the cation. Therefore, SDFs validify the investigated combined radial−radial distribution functions. Moreover, to have more visual clarity, we present the different atomistic interactions of solvents and anions with the Li cation in both the electrolytes, as presented in Figure 6.

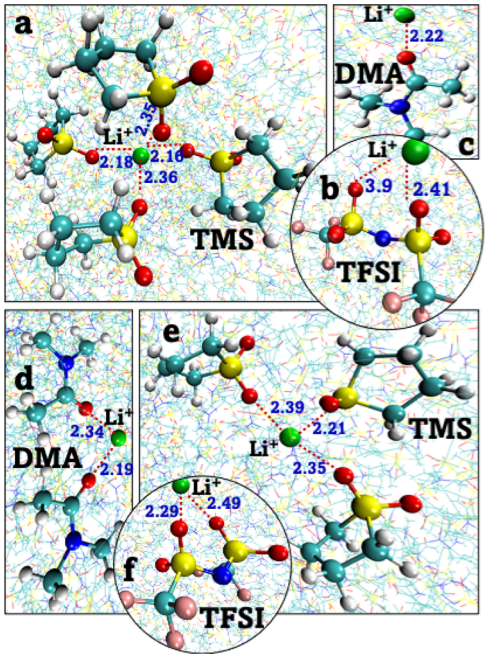


**Figure 6.** Interactions of $TFSI^-$, TMS, and DMA with the cation. Panels (a, b, and c) show the interactions of TMS, $TFSI^-$, and DMA with $Li^+$ for DMA/TMS (20:80). Panels (d, e, and f) show the interactions of DMA, TMS, and $TFSI^-$ with $Li^+$ for DMA/TMS (50:50). Distances are in Å unit.

**3.2. Diffusivity.** To get insight into the dynamics of the electrolytes, we computed the mean square displacements (MSDs) of each electrolytic component using the following equation:

$$\mathrm{MSD} = \frac{1}{N}\sum_{i=1}^{N}[r_i(t) - r_i(0)]^2 \tag{1}$$

where $r_i(t)$ denotes the position of the $i$th species at time $t$, whereas $r_i(0)$ is the initial position and $N$ is the total number of particles in the system. To conclude the diffusive regime, we explored the logarithm plot of MSDs and $\beta$ parameter. $\beta(t)$ is termed as

$$\beta(t) = \frac{\mathrm{dln}\langle \Delta r^2(t)\rangle}{\mathrm{dln}(t)} \tag{2}$$

where $\Delta r(t)$ expresses the change in the position of the particle as a function of time. In the diffusion region, the slope of the logarithm plot of the corresponding MSD becomes equal to 1 and the $\beta$ value approaches unity.[53,54] For a particle to enter into the diffusion regime, it must escape from its first solvation shell many times.[53,54] Figure 7 demonstrates the MSDs, log−log plots of MSDs, and $\beta(t)$ values for both electrolytes. For the DMA/TMS (20:80) electrolyte, $\beta(t)$ converges to unity between 30 and 90 ns, whereas for the DMA/TMS (50:50) system, we found 20 to 80 ns as the appropriate diffusion region (Figure 7c,f).

Figure 7a shows the sluggish movement of cations and anions, and this slow ionic mobility is due to the strong Coulombic interaction between the counterions. Despite being light and small, $Li^+$ is less mobile than $TFSI^-$ due to the very stable and bulkier solvation shell around it. Compared to salt counterparts, solvents have more freedom to move, as shown in Figure 7d. The lower molecular weight of DMA allows its faster dynamics than TMS in both solutions. However, the electrolyte with 50% DMA has more rapid kinetics than that with 20% DMA, and the reduced density could be one of the reasons. Moreover, a previous investigation[36] says that increasing the DMA content results in a significant decrease in viscosity. And this decrement in viscosity enhances the transportation and ionic conductivity of ionic species. To extract the self-diffusivity of electrolytic components, we employed Einstein's relation.[55,56] Table 2 shows the diffusion values calculated using the respective diffusive regime of MSDs using eq 3:

$$D_i = \frac{1}{6}\lim_{t\to\infty}\frac{\mathrm{d}}{\mathrm{d}t}\langle |r_i(t) - r_i(0)|^2\rangle \tag{3}$$

where $D_i$ is the self-diffusion coefficient and $r_i(t)$ and $r_i(0)$ indicate the positions of the particle at time = $t$ and time = 0. In DMA/TMS (50:50), the counterions diffuse faster than in DMA/TMS (20:80) electrolytes.

**3.3. Correlated and Uncorrelated Ionic Conductivities.** We computed the uncorrelated ionic conductivities (ICs) using the Nernst−Einstein[57,58] relation using eq 4:

$$\sigma_{NE} = \frac{N_i q_+ q_-}{K_B T V}(D^+ + D^-) \tag{4}$$

In the above equation, $\sigma_{NE}$ defines the uncorrelated ICs, $q_+$ and $q_-$ are the charges present on ions, $N_i$ is the number of LiTFSI in the system, $D^+$ and $D^-$ express the self-diffusion coefficients of counterions calculated from uncorrelated MSDs, $K_B$ denotes the Boltzmann constant, and $T$ and $V$ are the absolute temperature and volume, respectively. The Nernst−Einstein formula does not account for the ion−ion correlation.[59] In other words, the IC of particles calculated from the NE equation has no contributions from their neighboring particles. The ICs estimated using the NE relation suffer from substantial margins compared to experimental ICs. The Green−Kubo (CACF) relation[60] can be compared with the experimental IC data since it considers the correlation between ionic species.[61,62] This method[63,64] has been applied


https://doi.org/10.1021/acs.jpcb.2c07829
J. Phys. Chem. B 2023, 127, 2991−3000

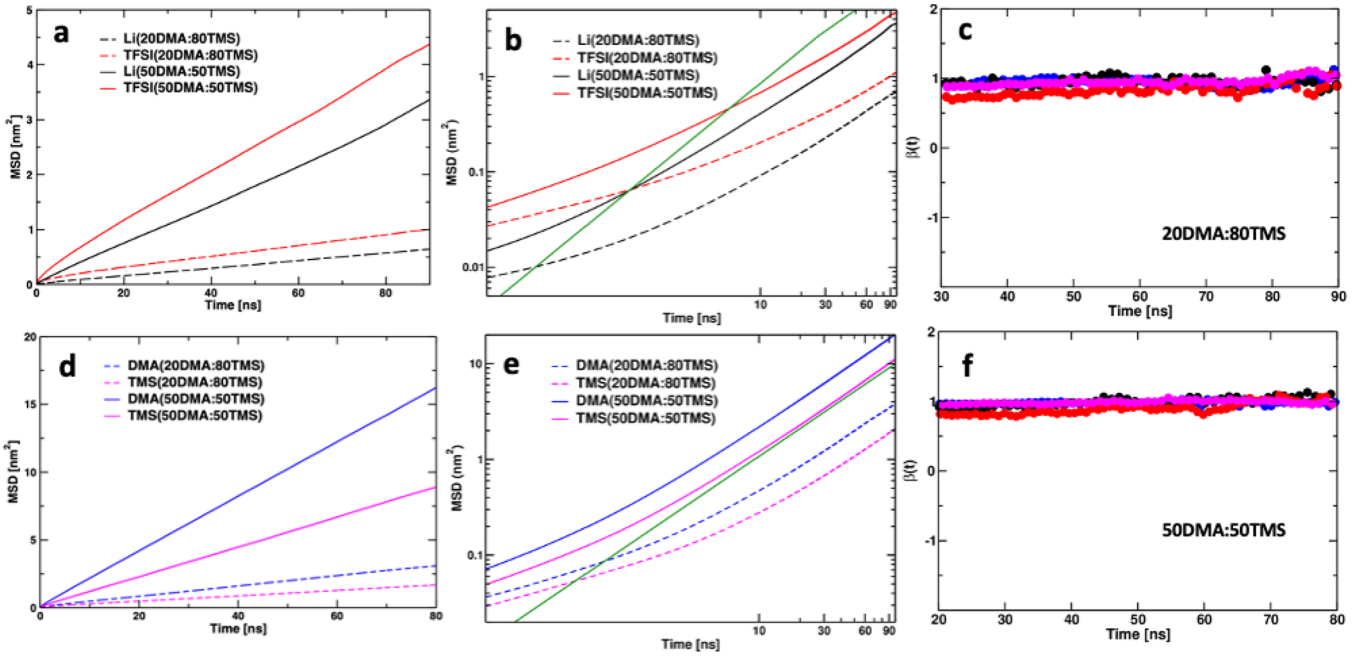


**Figure 7.** (a) MSDs of the cation and anion. (b) Logarithm plots of the cation and anion. (c) $\beta(t)$ parameter for 20DMA:80TMS. (d) MSDs of TMS and DMA. (e) Logarithm plots of TMS and DMA. (f) $\beta(t)$ parameter for 50DMA:50TMS. A line of slope 1 is added to the plot as a guide for the eyes. The diffusive region is from 30 to 90 ns for the 20:80 system and 20 to 80 ns for the 50:50 one.

**Table 2. Self-Diffusion Coefficients of Electrolytic Species for Both 20DMA:80TMS and 50DMA:50TMS Electrolytes**

| | $D$ [$10^{-11}$ m$^2$/s] | |
|---|---|---|
| electrolytic species | 20DMA:80TMS | 50DMA:50TMS |
| $Li^+$ | 0.69 | 3.57 |
| $TFSI^-$ | 0.98 | 4.53 |
| DMA | 3.71 | 20.04 |
| TMS | 2.01 | 11.07 |

to other systems with satisfactory results. The electric current autocorrelation function (CACF) is defined as

$$\mathrm{CACF}(t) = \sum_{i=1}^{N}\sum_{j=1}^{N} \langle q_i q_j V_i^c(t)\cdot V_j^c(0)\rangle \tag{5}$$

where $q_i$ and $q_j$ indicate the charges present on ions, whereas $V_i^c(t)$ and $V_j^c(0)$ express the COM velocity of ions. Integrating the CACF via the Green−Kubo (GK) equation gives the correlated ionic conductivity using eq 6:

$$\sigma = \frac{1}{3K_B TV}\int_0^{\infty} \sum_{i=1}^{N}\sum_{j=1}^{N} \langle q_i q_j V_i^c(t)\cdot V_j^c(0)\rangle \tag{6}$$

where $K_B$ denotes the Boltzmann constant and $T$ and $V$ are the absolute temperature and volume of the system, respectively. The obtained ICs using CACFs are in good agreement with the experiments. Our obtained value for IC 2.99 mS/cm for LiTFSI/20DMA:80TMS is close to that of the experimental IC, 3.02 mS/cm, while for LiTFSI/50DMA:50TMS, the reported value is 4.72 mS/cm, and the IC obtained from the GK method is 4.41 mS/cm. The computed conductivity for the 20DMA:80TMS system is almost similar to the experimental value; however, the IC for the 50DMA:50TMS system slightly deviates from the original data. Therefore, the dynamics uncover the correlation motion of ionic species. The ICs extracted from uncorrelated MSDs are insufficient for insight into the complex dynamics of ions in the electrolytes.

**3.4. Ion-Pair and Ion-Cage Formation.** In electrolytes, ions interact with counterions and solvents significantly in their solvation shells. These interactions affect the overall dynamics of the electrolytes. Moreover, ionic dynamics can be studied using the concept of ion-pair (IP) and ion-cage (IC) formation. To examine the ion-pair and ion-cage formation, we have followed the methodology used by Kirchner and coworkers.[65] For a selected pair to be called an ion pair, they should be at the minimum nearest distance to each other. To compute the dynamics of the ion pair and ion cage, the population variable $\beta_{ij}$ is used. The term $\beta_{ij} = 1$ if the ionic pair of interest is within the given cutoff distance (IC) or nearest neighbor (IP); otherwise, in the remaining cases, it switches to zero. The explanation we mention here for IP and IC resembles the earlier reports.[66,67] We computed the ion-pair and ion-cage lifetime from dimer existence autocorrelation functions (DACFs) using the TRAVIS software package.[52,65] The DACF is defined as

$$\mathrm{DACF}(\tau) = N\left\langle \sum_{t=0}^{T-\tau} \beta_{ij}(t+\tau)\cdot\beta_{ij}(t)\right\rangle_{i,j} \tag{7}$$

In eq 7, $T$ denotes the time, where $\tau$ is the increasing time and $\langle ... \rangle$ shows the average overall pair of interests. DACFs begin with unity; as $\tau$ increases, the autocorrelation function switches toward zero. The continuous[68] and intermittent[69] autocorrelation functions used to determine the lifetimes and relaxation time of hydrogen bonds between two species are employed in different systems where two moieties are involved for the calculations. Here, for continuous lifetimes, we investigated the continuous ion-pair $S_{IP}(t)$ and continuous ion-cage $S_{IC}(t)$ autocorrelation functions. For $S_{IP}(t)$, the initially formed ion pair cannot drift apart, which means that $\beta_{ij}$ remains unity until the ion pairs are closest to each other


https://doi.org/10.1021/acs.jpcb.2c07829
J. Phys. Chem. B 2023, 127, 2991−3000

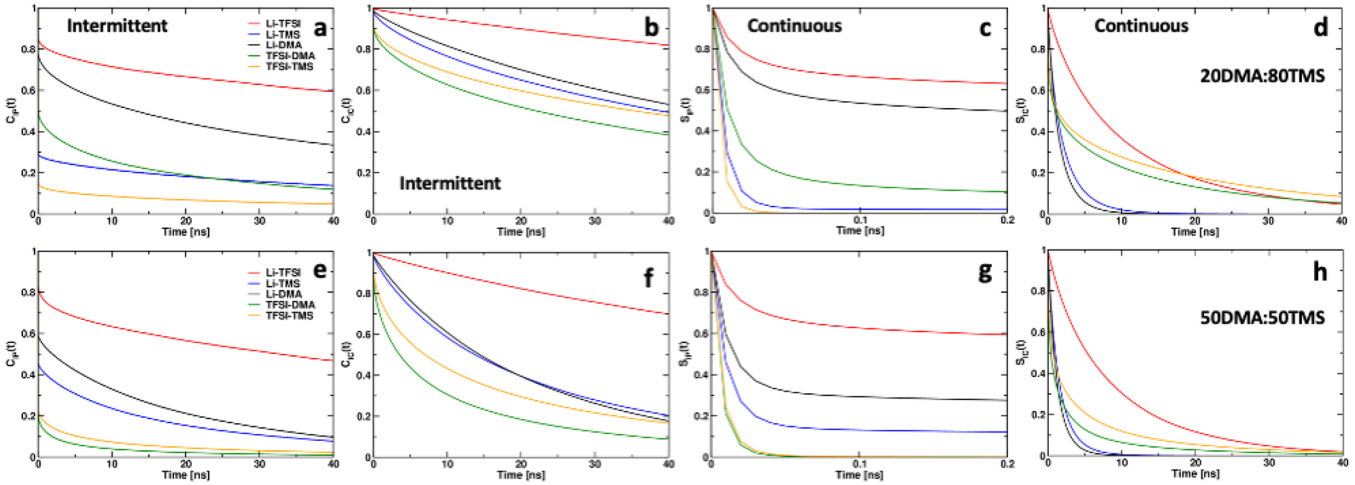


**Figure 8.** Autocorrelation functions for ion-pair/ion-solvent pair and ion-cage/ion-solvent cage. (a–d) For 20DMA:80TMS and (e–h) for 50DMA:50TMS. Panels (a, e) and (b, f) show the intermittent ion-pair/ion-solvent pair and intermittent ion-cage/ion-solvent cage correlation functions. Panels (c, g) and (d, h) indicate the continuous ion-pair/ion-solvent pair and continuous ion-cage/ion-solvent cage correlation functions.

**Table 3. Lifetimes (in ns) of Correlation Functions for Ion-Pair/Ion-Solvent Pair and Ion-Cage/Ion-Solvent Cage**

| electrolyte | pairs | continuous IC | intermittent IC | continuous IP | intermittent IP |
|---|---|---|---|---|---|
| 20DMA:80TMS | Li-TFSI | 16.3 | 1678.5 | 35.7 | 207.1 |
| | Li-DMA | 2.2 | 80.7 | 20.4 | 78.8 |
| | Li-TMS | 3.2 | 83.1 | 3.5 | 67.9 |
| | TFSI-DMA | 19.8 | 79.5 | 1.9 | 49.5 |
| | TFSI-TMS | 25.2 | 110.2 | 0.008 | 52.3 |
| 50DMA:50TMS | Li-TFSI | 11.7 | 131.5 | 27.3 | 106.9 |
| | Li-DMA | 1.8 | 26.6 | 8.4 | 26.0 |
| | Li-TMS | 2.5 | 34.3 | 2.9 | 31.6 |
| | TFSI-DMA | 13.1 | 28.9 | 0.04 | 11.2 |
| | TFSI-TMS | 15.1 | 41.0 | 0.005 | 31.1 |

and comes to zero in the remaining other cases. The way $S_{IC}(t)$ is defined, the counterions should not cross the first minima of COM RDFs to have the function $\beta_{ij}$ to be equal to 1. To calculate the intermittent lifetimes, intermittent ion-pair $C_{IP}(t)$[52,65−68,70,71] and intermittent ion-cage $C_{IC}(t)$[72,73] correlation functions are explored. The definitions for $C_{IP}(t)$ and $C_{IC}(t)$ differ from $S_{IP}(t)$ and $S_{IC}(t)$. In the case of $C_{IP}(t)$, the deformation of the ionic groups is allowed. $Li^+$ does not need to be continuously present at the nearest distance with $TFSI^-$. Likewise, for the intermittent $C_{IC}(t)$ function, the counterion can jump out of the cutoff distance and reestablish the ion cage with the same reference entity again.

The decay of ion-pair and ion-cage correlation functions is shown in Figure 8. Along with ion-pair and ion-cage correlation functions for the cation−anion, we also looked for cation−solvent and anion−solvent interactions. The fast decay of the ion pair is observed in contrast with the ion cage. In the ion cage, the cutoff distance is up to the first solvation shell, which takes a more extended period to decay. Moreover, for continuous correlations, if the considered pair moves apart from their nearest distance gap or crosses the cutoff limit, their reformation is not permitted, resulting in quick decay. But the intermittent functions care for the reformation phenomena; that is why intermittent functions decay slower than continuous ones. Similar to the previous investigation,[73] we also find the inverse relationship between conductivity and IP/IC. Faster decay of a correlation function results in enhanced dynamics of the system. We integrated the correlation functions to compute the lifetime of ion-pair and ion-cage formation. We checked the fitting of autocorrelation decay up to the triexponential functions. And we extracted the lifetimes of IP and IC using the triexponential process since it was found to give a better fit with the decaying curves of autocorrelation functions and present ion-pair and ion-cage lifetimes in Table 3. In both the electrolytes, with 1 M LiTFSI in 20DMA:80TMS and 50DMA:50TMS, the lifetimes of $S_{IP}(t)$ and $S_{IC}(t)$ are much smaller in comparison to those of $C_{IP}(t)$ and $C_{IC}(t)$, and this difference is attributed to the definition opted for these time-dependent functions. Out of all cases, the Li-TFSI pair shows the slowest decay; this again manifests the strong Coulomb force present between the ions. In the 50DMA:50TMS case, the anions/solvents interacting with $Li^+$ in the first solvation shell decay faster than in the case of 20DMA:80TMS. Similarly, the anion−solvent pair and anion−solvent cage also reveal the faster dynamics for the electrolyte with 50% DMA. Therefore, our investigation of these time-dependent autocorrelation functions supports the conductivity extracted from computation and experiments.

## 4. CONCLUSIONS

We have reported the structure and dynamics of electrolytes containing 1 M LiTFSI in DMA/TMS at two different compositions (20DMA:80TMS and 50DMA:50TMS, % v/v). We modeled the electrolytes using classical MD simulations to reveal the electrolyte's atomic-level details and establish the relation between the macroscopic dynamic properties with the



https://doi.org/10.1021/acs.jpcb.2c07829
J. Phys. Chem. B 2023, 127, 2991−3000

microscopic process of ion pairing and ion caging. We find minor structural changes in changing the DMA content from 20 to 50% in the electrolyte, emphasizing that the interactions of anions/solvents for the reference cation remain almost unaltered in both compositions. Out of all species, the TFSI anion has maximum occurrence in both solutions around the cation, and the order follows $TFSI^-$ > TMS > DMA. The CN remains almost the same (∼6) in both cases. TMS molecules contribute the most to the first coordination spheres around $Li^+$. The selection of the proper diffusive regime from simulations aided in calculating the self-diffusion coefficients of individual species. Ions and solvents of the DMA/TMS (50:50) electrolyte have faster diffusivity than that of the DMA/TMS (20:80) electrolyte. The conductivities computed from the GK equation, which considers the ionic correlation, match the experiments. The calculated continuous and intermittent correlation functions linearly vary with the inverse of ionic conductivity. The lifetimes were calculated by fitting the triexponential function to correlation decay. Along with ionic conductivities, the lifetimes of the ion pair and ion cage support the rapid dynamics of the 50DMA:50TMS electrolyte compared to the 20DMA:80TMS electrolyte. Therefore, our analysis may help to understand the microlevel configurations and dynamics of the electrolytes and provide scope to tune the performance of electrolytes to design better batteries.

## AUTHOR INFORMATION


### Corresponding Author

**Bhabani S. Mallik** − *Department of Chemistry, Indian Institute of Technology Hyderabad, Sangareddy 502285 Telangana, India;* orcid.org/0000-0001-9657-1497; Email: bhabani@chy.iith.ac.in

### Author

**Dhananjay** − *Department of Chemistry, Indian Institute of Technology Hyderabad, Sangareddy 502285 Telangana, India*

Complete contact information is available at: https://pubs.acs.org/10.1021/acs.jpcb.2c07829


### Notes

The authors declare no competing financial interest.

## ACKNOWLEDGMENTS

The financial support (DST/NSM/R&D_HPC_Applications/Sanction/2021/06) for this work was provided by the National Supercomputing Mission (NSM), India. The authors acknowledge the help of Ritesh Goutam Nayak during the initial stage of the work.

## REFERENCES


(1) Yang, Z.; Zhang, J.; Kintner-Meyer, M. C. W.; Lu, X.; Choi, D.; Lemmon, J. P.; Liu, J. Electrochemical Energy Storage for Green Grid. *Chem. Rev.* **2011**, *111*, 3577−3613.

(2) Larcher, D.; Tarascon, J.-M. Towards Greener and More Sustainable Batteries for Electrical Energy Storage. *Nat. Chem.* **2015**, *7*, 19−29.

(3) Christensen, J.; Albertus, P.; Sanchez-Carrera, R. S.; Lohmann, T.; Kozinsky, B.; Liedtke, R.; Ahmed, J.; Kojic, A. A Critical Review of Li/Air Batteries. *J. Electrochem. Soc.* **2011**, *159*, R1−R30.

(4) Bhatt, M. D.; Geaney, H.; Nolan, M.; O'Dwyer, C. Key Scientific Challenges in Current Rechargeable Non-Aqueous Li−O2 Batteries: Experiment and Theory. *Phys. Chem. Chem. Phys.* **2014**, *16*, 12093−12130.

(5) Luntz, A. C.; McCloskey, B. D. Nonaqueous Li−Air Batteries: A Status Report. *Chem. Rev.* **2014**, *114*, 11721−11750.

(6) Wang, L.; Peng, Z.-Q. Characterization of An Oxygen Evolution Reaction Redox Mediator for Li-O2 Battery by In-Situ Differential Electrochemical Mass Spectrometry. *Chin. J. Anal. Chem.* **2020**, *48*, e20165−e20171.

(7) Xu, Y.-F.; Chen, Y.; Xu, G.-L.; Zhang, X.-R.; Chen, Z.; Li, J.-T.; Huang, L.; Amine, K.; Sun, S.-G. RuO2 Nanoparticles Supported on MnO2 Nanorods as High Efficient Bifunctional Electrocatalyst of Lithium-Oxygen Battery. *Nano Energy* **2016**, *28*, 63−70.

(8) Lu, Y.-C.; Gasteiger, H. A.; Shao-Horn, Y. Catalytic Activity Trends of Oxygen Reduction Reaction for Nonaqueous Li-Air Batteries. *J. Am. Chem. Soc.* **2011**, *133*, 19048−19051.

(9) Cheng, F.; Chen, J. Metal−Air Batteries: From Oxygen Reduction Electrochemistry to Cathode Catalysts. *Chem. Soc. Rev.* **2012**, *41*, 2172−2192.

(10) Feng, S.; Chen, M.; Giordano, L.; Huang, M.; Zhang, W.; Amanchukwu, C. V.; Anandakathir, R.; Shao-Horn, Y.; Johnson, J. A. Mapping a Stable Solvent Structure Landscape for Aprotic Li−Air Battery Organic Electrolytes. *J. Mater. Chem. A* **2017**, *5*, 23987−23998.

(11) Mizuno, F.; Nakanishi, S.; Kotani, Y.; Yokoishi, S.; Iba, H. Rechargeable Li-Air Batteries with Carbonate-Based Liquid Electrolytes. *Electrochemistry* **2010**, *78*, 403−405.

(12) Bryantsev, V. S.; Blanco, M. Computational Study of the Mechanisms of Superoxide-Induced Decomposition of Organic Carbonate-Based Electrolytes. *J. Phys. Chem. Lett.* **2011**, *2*, 379−383.

(13) Xu, W.; Xu, K.; Viswanathan, V. V.; Towne, S. A.; Hardy, J. S.; Xiao, J.; Nie, Z.; Hu, D.; Wang, D.; Zhang, J.-G. Reaction Mechanisms for the Limited Reversibility of Li−O2 Chemistry in Organic Carbonate Electrolytes. *J. Power Sources* **2011**, *196*, 9631−9639.

(14) Freunberger, S. A.; Chen, Y.; Peng, Z.; Griffin, J. M.; Hardwick, L. J.; Bardé, F.; Novák, P.; Bruce, P. G. Reactions in the Rechargeable Lithium−O2 Battery with Alkyl Carbonate Electrolytes. *J. Am. Chem. Soc.* **2011**, *133*, 8040−8047.

(15) McCloskey, B. D.; Bethune, D. S.; Shelby, R. M.; Mori, T.; Scheffler, R.; Speidel, A.; Sherwood, M.; Luntz, A. C. Limitations in Rechargeability of Li-O2 Batteries and Possible Origins. *J. Phys. Chem. Lett.* **2012**, *3*, 3043−3047.

(16) Ryan, K. R.; Trahey, L.; Ingram, B. J.; Burrell, A. K. Limited Stability of Ether-Based Solvents in Lithium−Oxygen Batteries. *J. Phys. Chem. C* **2012**, *116*, 19724−19728.

(17) Freunberger, S. A.; Chen, Y.; Drewett, N. E.; Hardwick, L. J.; Bardé, F.; Bruce, P. G. The Lithium−Oxygen Battery with Ether-Based Electrolytes. *Angew. Chem., Int. Ed.* **2011**, *50*, 8609−8613.

(18) Monaco, S.; Soavi, F.; Mastragostino, M. Role of Oxygen Mass Transport in Rechargeable Li/O2 Batteries Operating with Ionic Liquids. *J. Phys. Chem. Lett.* **2013**, *4*, 1379−1382.

(19) Cai, K.; Pu, W.; Gao, Y.; Hou, J.; Deng, C.; Wang, C.; Mao, Z. Investigation of Ionic Liquid Composite Electrolyte for Lithium−Oxygen Battery. *Int. J. Hydrogen Energy* **2013**, *38*, 11023−11027.

(20) Elia, G. A.; Hassoun, J.; Kwak, W.-J.; Sun, Y.-K.; Scrosati, B.; Mueller, F.; Bresser, D.; Passerini, S.; Oberhumer, P.; Tsiouvaras, N.; Reiter, J. An Advanced Lithium−Air Battery Exploiting an Ionic Liquid-Based Electrolyte. *Nano Lett.* **2014**, *14*, 6572−6577.

(21) Bryantsev, V. S.; Giordani, V.; Walker, W.; Blanco, M.; Zecevic, S.; Sasaki, K.; Uddin, J.; Addison, D.; Chase, G. V. Predicting Solvent Stability in Aprotic Electrolyte Li−Air Batteries: Nucleophilic Substitution by the Superoxide Anion Radical (O2•−). *J. Phys. Chem. A* **2011**, *115*, 12399−12409.

(22) Walker, W.; Giordani, V.; Uddin, J.; Bryantsev, V. S.; Chase, G. V.; Addison, D. A Rechargeable Li−O2 Battery Using a Lithium Nitrate/N N-Dimethylacetamide Electrolyte. *J. Am. Chem. Soc.* **2013**, *135*, 2076−2079.

(23) Bryantsev, V. S.; Giordani, V.; Walker, W.; Uddin, J.; Lee, I.; van Duin, A. C. T.; Chase, G. V.; Addison, D. Investigation of Fluorinated Amides for Solid−Electrolyte Interphase Stabilization in

Li−O2 Batteries Using Amide-Based Electrolytes. *J. Phys. Chem. C* **2013**, *117*, 11977−11988.
(24) Xu, D.; Wang, Z.; Xu, J.; Zhang, L.; Zhang, X. Novel DMSO-Based Electrolyte for High Performance Rechargeable Li−O2 Batteries. *Chem. Commun.* **2012**, *48*, 6948−6950.
(25) Sharon, D.; Afri, M.; Noked, M.; Garsuch, A.; Frimer, A. A.; Aurbach, D. Oxidation of Dimethyl Sulfoxide Solutions by Electrochemical Reduction of Oxygen. *J. Phys. Chem. Lett.* **2013**, *4*, 3115−3119.
(26) Takechi, K.; Higashi, S.; Mizuno, F.; Nishikoori, H.; Iba, H.; Shiga, T. Stability of Solvents against Superoxide Radical Species for the Electrolyte of Lithium-Air Battery. *ECS Electrochem. Lett.* **2012**, *1*, A27−A29.
(27) Balaish, M.; Kraytsberg, A.; Ein-Eli, Y. A Critical Review on Lithium−Air Battery Electrolytes. *Phys. Chem. Chem. Phys.* **2014**, *16*, 2801−2822.
(28) Morita, M.; Tachihara, F.; Matsuda, Y. Dimethyl Sulfoxide-Based Electrolytes for Rechargeable Lithium Batteries. *Electrochim. Acta* **1987**, *32*, 299−305.
(29) Liang, C.; Wang, F.; Xu, Y.; Chen, J.; Liu, D.; Luo, Z. A Stable Electrolyte Makes a Nonaqueous Li−O2 Battery Truly Rechargeable. *New J. Chem.* **2013**, *37*, 2568.
(30) Xu, D.; Wang, Z.; Xu, J.; Zhang, L.; Wang, L.; Zhang, X. A Stable Sulfone Based Electrolyte for High Performance Rechargeable Li−O2 Batteries. *Chem. Commun.* **2012**, *48*, 11674−11676.
(31) Luo, Z.-K.; Liang, C.-S.; Wang, F.; Xu, Y.-H.; Chen, J.; Liu, D.; Sun, H.-Y.; Yang, H.; Fan, X.-P. Optimizing Main Materials for a Lithium-Air Battery of High Cycle Life. *Adv. Funct. Mater.* **2014**, *24*, 2101−2105.
(32) Ferrari, S.; Quartarone, E.; Tomasi, C.; Bini, M.; Galinetto, P.; Fagnoni, M.; Mustarelli, P. Investigation of Ether-Based Ionic Liquid Electrolytes for Lithium-O2 Batteries. *J. Electrochem. Soc.* **2014**, *162*, A3001.
(33) Herranz, J.; Garsuch, A.; Gasteiger, H. A. Using Rotating Ring Disc Electrode Voltammetry to Quantify the Superoxide Radical Stability of Aprotic Li−Air Battery Electrolytes. *J. Phys. Chem. C* **2012**, *116*, 19084−19094.
(34) Cecchetto, L.; Salomon, M.; Scrosati, B.; Croce, F. Study of a Li-Air Battery Having an Electrolyte Solution Formed by a Mixture of an Ether-Based Aprotic Solvent and an Ionic Liquid. *J. Power Sources* **2012**, *213*, 233−238.
(35) Xu, W.; Xiao, J.; Zhang, J.; Wang, D.; Zhang, J.-G. Optimization of Nonaqueous Electrolytes for Primary Lithium/Air Batteries Operated in Ambient Environment. *J. Electrochem. Soc.* **2009**, *156*, A773.
(36) Wang, F.; Chen, H.; Wu, Q.; Mei, R.; Huang, Y.; Li, X.; Luo, Z. Study on the Mixed Electrolyte of N,N-Dimethylacetamide/Sulfolane and Its Application in Aprotic Lithium−Air Batteries. *ACS Omega* **2017**, *2*, 236−242.
(37) Martínez, L.; Andrade, R.; Birgin, E. G.; Martínez, J. M. PACKMOL: A package for building initial configurations for molecular dynamics simulations. *J. Comput. Chem.* **2009**, *30*, 2157−2164.
(38) Lee, C.; Yang, W.; Parr, R. G. Development of the Colle-Salvetti Correlation-Energy Formula into a Functional of the Electron Density. *Phys. Rev. B* **1988**, *37*, 785−789.
(39) Becke, A. D. Density-functional Thermochemistry. III. The Role of Exact Exchange. *J. Chem. Phys.* **1993**, *98*, 5648−5652.
(40) Stephens, P. J.; Devlin, F. J.; Chabalowski, C. F.; Frisch, M. J. Ab Initio Calculation of Vibrational Absorption and Circular Dichroism Spectra Using Density Functional Force Fields. *J. Phys. Chem.* **1994**, *98*, 11623−11627.
(41) Frisch, M.; Trucks, G. W.; Schlegel, H. B.; Scuseria, G. E.; Robb, M. A.; Cheeseman, J. R.; Scalmani, G.; Barone, V.; Mennucci, B.; Petersson, G. A., et al. *Gaussian 09*; Gaussian, Inc. Wallingford, CT, 2009.
(42) Van Der Spoel, D.; Lindahl, E.; Hess, B.; Groenhof, G.; Mark, A. E.; Berendsen, H. J. C. GROMACS: Fast, Flexible, and Free. *J. Comput. Chem.* **2005**, *26*, 1701−1718.
(43) Abraham, M. J.; Murtola, T.; Schulz, R.; Páll, S.; Smith, J. C.; Hess, B.; Lindahl, E. GROMACS: High Performance Molecular Simulations through Multi-Level Parallelism from Laptops to Supercomputers. *SoftwareX* **2015**, *1-2*, 19.
(44) Jorgensen, W. L.; Tirado-Rives, J. The OPLS [Optimized Potentials for Liquid Simulations] Potential Functions for Proteins, Energy Minimizations for Crystals of Cyclic Peptides and Crambin. *J. Am. Chem. Soc.* **1988**, *110*, 1657−1666.
(45) Jorgensen, W. L.; Maxwell, D. S.; Tirado-Rives, J. Development and Testing of the OPLS All-Atom Force Field on Conformational Energetics and Properties of Organic Liquids. *J. Am. Chem. Soc.* **1996**, *118*, 11225−11236.
(46) Lee, S. H.; Rasaiah, J. C. Molecular Dynamics Simulation of Ion Mobility. 2. Alkali Metal and Halide Ions Using the SPC/E Model for Water at 25 °C. *J. Phys. Chem.* **1996**, *100*, 1420−1425.
(47) Bayly, C. I.; Cieplak, P.; Cornell, W.; Kollman, P. A. A Well-Behaved Electrostatic Potential Based Method Using Charge Restraints for Deriving Atomic Charges: The RESP Model. *J. Phys. Chem.* **1993**, *97*, 10269−10280.
(48) Wang, J.; Wang, W.; Kollman, P. A.; Case, D. A. Automatic Atom Type and Bond Type Perception in Molecular Mechanical Calculations. *J. Mol. Graphics Modell.* **2006**, *25*, 247−260.
(49) Bussi, G.; Donadio, D.; Parrinello, M. Canonical Sampling through Velocity Rescaling. *J. Chem. Phys.* **2007**, *126*, No. 014101.
(50) Molecular Dynamics with Coupling to an External Bath. *J. Chem. Phys.* **1984**, *81* (), 3684−3690, DOI: 10.1063/1.448118.
(51) Kumar, G.; Kartha, T. R.; Mallik, B. S. Novelty of Lithium Salt Solution in Sulfone and Dimethyl Carbonate-Based Electrolytes for Lithium-Ion Batteries: A Classical Molecular Dynamics Simulation Study of Optimal Ion Diffusion. *J. Phys. Chem. C* **2018**, *122*, 26315−26325.
(52) Brehm, M.; Kirchner, B. TRAVIS - A Free Analyzer and Visualizer for Monte Carlo and Molecular Dynamics Trajectories. *J. Chem. Inf. Model.* **2011**, *51*, 2007−2023.
(53) Del Pópolo, M. G.; Voth, G. A. On the Structure and Dynamics of Ionic Liquids. *J. Phys. Chem. B* **2004**, *108*, 1744−1752.
(54) Mallik, B. S.; Siepmann, J. I. Thermodynamic, Structural and Transport Properties of Tetramethyl Ammonium Fluoride: First Principles Molecular Dynamics Simulations of an Unusual Ionic Liquid. *J. Phys. Chem. B* **2010**, *114*, 12577−12584.
(55) Jiang, W.; Yan, T.; Wang, Y.; Voth, G. A. Molecular Dynamics Simulation of the Energetic Room-Temperature Ionic Liquid, 1-Hydroxyethyl-4-Amino-1,2,4-Triazolium Nitrate (HEATN). *J. Phys. Chem. B* **2008**, *112*, 3121−3131.
(56) Sarangi, S. S.; Zhao, W.; Müller-Plathe, F.; Balasubramanian, S. Correlation between Dynamic Heterogeneity and Local Structure in a Room-Temperature Ionic Liquid: A Molecular Dynamics Study of [Bmim][PF6]. *ChemPhysChem* **2010**, *11*, 2001−2010.
(57) Araque, J. C.; Hettige, J. J.; Margulis, C. J. Ionic Liquids—Conventional Solvent Mixtures, Structurally Different but Dynamically Similar. *J. Chem. Phys.* **2015**, *143*, No. 134505.
(58) Chintapalli, M.; Timachova, K.; Olson, K. R.; Mecham, S. J.; Devaux, D.; DeSimone, J. M.; Balsara, N. P. Relationship between Conductivity, Ion Diffusion, and Transference Number in Perfluoropolyether Electrolytes. *Macromolecules* **2016**, *49*, 3508−3515.
(59) Yllö, A.; Zhang, C. Experimental and Molecular Dynamics Study of the Ionic Conductivity in Aqueous LiCl Electrolytes. *Chem. Phys. Lett.* **2019**, *729*, 6−10.
(60) Harada, M.; Yamanaka, A.; Tanigaki, M.; Tada, Y. Mass and Size Effects on the Transport Properties of Molten Salts. *J. Chem. Phys.* **1982**, *76*, 1550−1556.
(61) Kowsari, M. H.; Alavi, S.; Ashrafizaadeh, M.; Najafi, B. Molecular Dynamics Simulation of Imidazolium-Based Ionic Liquids II. Transport Coefficients. *J. Chem. Phys.* **2009**, *130*, No. 014703.
(62) Kowsari, M. H.; Alavi, S.; Najafi, B.; Gholizadeh, K.; Dehghanpisheh, E.; Ranjbar, F. Molecular Dynamics Simulations of the Structure and Transport Properties of Tetra-Butylphosphonium Amino Acid Ionic Liquids. *Phys. Chem. Chem. Phys.* **2011**, *13*, 8826−8837.


https://doi.org/10.1021/acs.jpcb.2c07829
J. Phys. Chem. B 2023, 127, 2991−3000

(63) Reddy, T. D. N.; Mallik, B. S. Solvent-Assisted Li-Ion Transport and Structural Heterogeneity in Fluorinated Battery Electrolytes. *J. Phys. Chem. B* **2021**, *125*, 10551−10561.
(64) Reddy, T. D. N.; Mallik, B. S. Connecting Correlated and Uncorrelated Transport to Dynamics of Ionic Interactions in Cyclic Ammonium-Based Ionic Liquids. *J. Phys. Chem. B* **2020**, *124*, 6813−6824.
(65) Gehrke, S.; Von Domaros, M.; Clark, R.; Hollóczki, O.; Brehm, M.; Welton, T.; Luzar, A.; Kirchner, B. Structure and Lifetimes in Ionic Liquids and Their Mixtures. *Faraday Discuss.* **2018**, *206*, 219−245.
(66) Chandra, A. Effects of Ion Atmosphere on Hydrogen-Bond Dynamics in Aqueous Electrolyte Solutions. *Phys. Rev. Lett.* **2000**, *85*, 768−771.
(67) Mallik, B. S.; Chandra, A. Hydrogen Bond and Residence Dynamics of Ion−Water and Water−Water Pairs in Supercritical Aqueous Ionic Solutions: Dependence on Ion Size and Density. *J. Chem. Phys.* **2006**, *125*, No. 234502.
(68) Balasubramanian, S.; Pal, S.; Bagchi, B. Hydrogen-Bond Dynamics near a Micellar Surface: Origin of the Universal Slow Relaxation at Complex Aqueous Interfaces. *Phys. Rev. Lett.* **2002**, *89*, No. 115505.
(69) Rawat, N.; Biswas, P. Hydrogen Bond Dynamics in Intrinsically Disordered Proteins. *J. Phys. Chem. B* **2014**, *118*, 3018−3025.
(70) Luzar, A.; Chandler, D. Hydrogen-Bond Kinetics in Liquid Water. *Nature* **1996**, *379*, 55−57.
(71) Koneshan, S.; Rasaiah, J. C.; Dang, L. X. Computer Simulation Studies of Aqueous Solutions at Ambient and Supercritical Conditions Using Effective Pair Potential and Polarizable Potential Models for Water. *J. Chem. Phys.* **2001**, *114*, 7544−7555.
(72) van der Spoel, D.; van Maaren, P. J.; Larsson, P.; Têmneanu, N. Thermodynamics of Hydrogen Bonding in Hydrophilic and Hydrophobic Media. *J. Phys. Chem. B* **2006**, *110*, 4393−4398.
(73) Zhang, Y.; Maginn, E. J. Direct Correlation between Ionic Liquid Transport Properties and Ion Pair Lifetimes: A Molecular Dynamics Study. *J. Phys. Chem. Lett.* **2015**, *6*, 700−705.




https://doi.org/10.1021/acs.jpcb.2c07829
J. Phys. Chem. B 2023, 127, 2991−3000